

H α emitting galaxies and the star formation rate density at $z \simeq 0.24$

S. Pascual¹, J. Gallego¹, A. Aragón-Salamanca², and J. Zamorano¹

¹ Departamento de Astrofísica, Facultad de C.C Físicas, Universidad Complutense de Madrid, E-28040, Madrid, Spain

² School of Physics and Astronomy, University of Nottingham, University Park, Nottingham NG7 2RD, UK

Received August 9, 2001; accepted September 20, 2001

Abstract. We have carried out a survey searching for H α emitting galaxies at $z \simeq 0.24$ using a narrow band filter tuned with the redshifted line. The total sky area covered was 0.19 square degrees within the redshift range 0.228 to 0.255 in a set of four fields in the ELAIS-N1 zone. This corresponds to a volume of $9.8 \cdot 10^3 \text{ Mpc}^3$ and a look-back time of 3.6 Gyr when $H_0 = 50 \text{ km s}^{-1} \text{ Mpc}^{-1}$ and $q_0 = 0.5$ are assumed. A total of 52 objects are selected as candidates for a broad band limiting magnitude of $I \sim 22.9$, plus 16 detected only in the narrow band image for a narrow band limiting magnitude for object detection of 21.0. The threshold detection corresponds to about 20 \AA equivalent width with an uncertainty of $\sim \pm 10 \text{ \AA}$. Point-like objects (15) were excluded from our analysis using CLASS_STAR parameter from SExtractor. The contamination from other emission lines such as [O II] $\lambda 3727$, H β and [O III] $\lambda \lambda 4959, 5007$ at redshifts 1.2, 0.66 and 0.61 respectively is estimated, and found to be negligible at the flux limits of our sample. We find an extinction-corrected H α luminosity density of $(5.4 \pm 1.1) \cdot 10^{39} \text{ erg s}^{-1} \text{ Mpc}^{-3}$. This uncertainty takes into account the photometric and Poissonian errors only. Assuming a constant relation between the H α luminosity and star formation rate, the SFR density in the covered volume is $(0.043 \pm 0.009) \text{ M}_{\odot} \text{ yr}^{-1} \text{ Mpc}^{-3}$. This translates to $(0.037 \pm 0.009) \text{ M}_{\odot} \text{ yr}^{-1} \text{ Mpc}^{-3}$ when the total density is corrected for the AGN contribution as estimated in the local Universe. This value is a factor ~ 4 higher than the local SFR density. This result needs to be confirmed by future spectroscopic follow-up observations.

Key words. Galaxies: distances and redshifts – Galaxies: evolution – Galaxies: luminosity function, mass function

1. Introduction

The star formation rate density of the Universe is one of the key observables needed for our understanding of galaxy formation and evolution. In a key reference paper, Madau et al. (1996) connected the high-redshift luminosity density obtained from the coaddition of the emission from individually-detected galaxies with that obtained from low redshift surveys. This luminosity density was then translated into a star formation rate (SFR) density. Their original SFR density versus redshift plot showed that the SFR density steeply increases from $z \sim 0$ to $z \sim 1$ and decreased beyond $z \simeq 2.5$, suggesting that it probably peaked between $z \simeq 1$ and $z \simeq 2$. Deep redshift surveys also suggest that the star-formation activity substantially increases with redshift until $z \simeq 1$ (Songaila et al. 1994; Ellis et al. 1996; Lilly et al. 1996; Hammer et al. 1997; Hogg et al. 1998). However, the high redshift behaviour is not so clear, and the decline in SFR density beyond $z \sim 2$ is still contentious.

Detailed theoretical works are starting to shed light to the problem. It is now possible to build models which, within the hierarchical clustering scenario, put together dark matter, gas and stars (e.g., Lacey & Silk 1991; Kauffmann et al. 1993, 1994, 1999; Cole et al. 1994). These models can provide a reasonable match to both the present-day characteristics of galaxies (Baugh et al. 1998), as well as the properties of galaxies at high redshift (Somerville & Primack 1998; Somerville et al. 2001). These models are also able to quantitatively predict the global star formation history of the Universe, i.e. the comoving number density of galaxies as a function of star formation rate, and as a function of redshift.

One of the major problems that arises when analysing galaxy populations at different redshifts is how to make a meaningful comparison. To test directly whether substantial evolution in the star-formation activity has occurred, we need to measure the SFR density of the Universe at different redshifts using similar techniques. Optimally, we should try to use the same selection criteria, same galaxy populations and same SFR tracer. Such a uniform mea-

surement would provide a much stronger constraint for galaxy formation and evolution models.

The H α luminosity, related to the number of massive stars, is a direct measurement of the current star formation rate (modulo the Initial Mass Function). Metallic nebular lines such as [O II] λ 3727 and [O III] λ 4959, 5007 (affected by excitation and metallicity) and far-IR fluxes (affected by dust abundance and properties) are star-formation *indicators* rather than *quantitative* measurements (see, e.g., Gallagher et al. 1989; Kennicutt 1992a). Thus the best way to quantify current star formation is by using an H α selected sample of galaxies (Charlot 1998). Although star formation in heavily obscured regions will not be revealed by H α , if we select the galaxies with the same criteria at all redshifts, the samples –and the derived SFRs– will be directly comparable.

A few pioneering works have estimated average SFR densities measuring H α luminosities in the near-infrared for small samples below $z=1$ (Jones & Bland-Hawthorn 2001, using tunable filters), at $z\sim 1$ (Glazebrook et al. 1999; Yan et al. 1999) and $z\sim 2$ (Iwamuro et al. 2000; Moorwood et al. 2000; van der Werf et al. 2000), and H β luminosities for samples of 5 and 19 objects at $z\sim 3$ (Pettini et al. 1998, 2001). These preliminary results indicate that SFRs from Balmer lines follow the general trend traced by UV broad-band luminosities at high redshifts. They are found to be $2\text{--}3\times$ higher than those inferred from the extinction corrected UV at all redshifts. The UV flux comes from the OB stars on the star-forming region and the underlying population whereas the H α flux comes from the H II region surrounding the OB stars. The different origin of the radiation explains the different measured SFRs.

A $z\sim 0$ benchmark in this field is the SFR density obtained from the Universidad Complutense de Madrid survey of H α emission line galaxies in the local Universe (Gallego et al. 1995). At $z\sim 0.2$, the only available H α luminosity function is the one obtained for the broad-band selected CFRS sample (Tresse & Maddox 1998). In this paper we describe a survey for H α emitting galaxies at $z\sim 0.24$ carried out with a narrow band filter.

Section 2 describes the data acquisition and the image reduction; Section 3 shows the galaxy selection process; in Sect. 4 we calculate the H α luminosity function and the SFR density, and finally in Sect. 5 the conclusions are presented. All along the paper we assume a Friedman model cosmology (cosmological constant $\Lambda_0=0$) with a Hubble constant $H_0=50\text{ km s}^{-1}\text{ Mpc}^{-1}$ and deceleration parameter $q_0=0.5$.

2. Data acquisition and reduction

Our survey for H α emitting galaxies was carried out using the focal reducer CAFOS¹ at the 2.2m telescope in CAHA (Centro Astronómico Hispano-Alemán, Almería, Spain).

Table 1. Survey fields

Field Name	RA	Dec	Exposures (s)	
	(J2000)	(J2000)	I	NB
ELAIS a3	16:05:30	+54:30:36	600	3000
ELAIS a4	16:04:00	+54:30:36	600	6000
ELAIS b3	16:06:15	+54:17:36	600	5000
ELAIS b4	16:04:45	+54:17:36	600	4000

This instrument is equipped with a 2048×2048 Site#1d CCD with $24\mu\text{m}$ pixels ($0''.53$ on the sky), which covers a circular area of $16'$ diameter. In the data reduction process, the covered area is reduced to $14'.6$. Four fields were observed, all of them located near the centre of the European Large-Area ISO Survey field ELAIS-N1 (Rowan-Robinson et al. 1999; Oliver et al. 2000). Our strategy was to observe overlapping regions between the fields, so we can have consistent photometry on all the frames. All four fields were observed through a 16 nm FWHM narrow band filter centred at 816 nm, in a region of low OH emission. Broad band *I*-filter images were also obtained. The filters used were, respectively, 816/16 and 850/150c in the CAHA filters database.

Of the four observing nights, two were lost due to Sahara's dust on the atmosphere. The other two nights had non-photometric conditions. The overall seeing was $1''.2$. Total exposures were 600s in the broad and 3000 – 6000s in the narrow filter. The survey covered 0.19 square degrees, corresponding to $9.8\cdot 10^3\text{ Mpc}^3$ comoving volume at $z=0.242$, given the width of the narrow-band filter. Table 1 shows the fields surveyed.

The images were processed using the standard reduction procedures for de-biasing and flat-fielding found in the CCDRED facility within IRAF². Fringing was present in the broad band images at $\sim 5\%$ of the sky level. It was removed by combining deep blank sky frames to obtain the fringe pattern, placing it at zero mean level, scaling it to the level of the sky background of the science frame, and subtracting. The frames were aligned using the coordinates of bright stars on the images before combining. Due to the use of the focal reducer, the borders of the frames suffer from geometrical distortion and it is not enough to apply a shift to align the images. We have applied a general transformation using shifts (about $30''$), rotation ($\sim 2\cdot 10^{-3}\%$) and re-scaling ($\sim 0.1\%$). Finally the frames were combined to obtain the final image for each filter used. The frames were scaled to a common count level using stars in the overlapping regions between the images. Because the nights were not photometric, photometric calibration was achieved using stars of the USNO-A2 catalogue (Monet et al. 1996) contained in our fields and using synthetic colours $B - R$ and $R - I$ calculated with template spectra from Pickles (1998). We estimate that the

² IRAF is distributed by the National Optical Astronomy Observatories, which is operated by the Association of Universities for Research in Astronomy, Inc. (AURA) under cooperative agreement with the National Science Foundation.

¹ <http://www.caha.es/CAHA/Instruments/index.html>

zero-point uncertainty is $\simeq 0.1$ mag. The zero-point of the narrow band calibration was obtained assuming a mean $I - m_{NB} = 0$, using the bright end of the selection diagrams (Figure 1).

3. Nature of candidates

3.1. Object detection and candidate selection

Catalogues of the objects in all the four surveyed fields were made using **SExtractor** (Bertin & Arnouts 1996). The objects are detected using the *double-image mode*: the narrow band frame is used as a reference image for detection and then the flux is summed up in 6 pixel diameter apertures in both the narrow- and broad-band image. This aperture size is $3''18$, i.e., $2.65 \times \text{FWHM}$ of the seeing, corresponding to 15 kpc at $z=0.242$.

Candidate line emitting objects were selected using their excess narrow versus broad flux on a plot of m_{NB} versus $I - m_{NB}$. For each candidate, both broad and narrow aperture fluxes, line equivalent width and the sigma excess are calculated. The flux density in each filter can be expressed as the sum of the line flux and the continuum flux density (the line is covered by both filters):

$$f_{\lambda}^B = f_{\lambda}^c + \frac{f_L}{\Delta_B} \quad f_{\lambda}^N = f_{\lambda}^c + \frac{f_L}{\Delta_N} \quad (1)$$

with f_{λ}^c the continuum flux; f_L the line flux; Δ_B and Δ_N the broad and narrow band filter effective widths and f_{λ}^B and f_{λ}^N the flux density in each filter. Then the line flux, continuum flux and equivalent width can be express as follows:

$$f_L = \Delta_N (f_{\lambda}^N - f_{\lambda}^B) \frac{1}{1 - \frac{\Delta_N}{\Delta_B}} \quad (2)$$

$$f_{\lambda}^c = f_{\lambda}^B \frac{1 - \frac{f_{\lambda}^N \Delta_N}{f_{\lambda}^B \Delta_B}}{1 - \frac{\Delta_N}{\Delta_B}} \quad (3)$$

$$EW = \frac{f_L}{f_{\lambda}^c} = \Delta_N \left(\frac{f_{\lambda}^N - f_{\lambda}^B}{f_{\lambda}^B} \right) \left(\frac{1}{1 - \frac{f_{\lambda}^N \Delta_N}{f_{\lambda}^B \Delta_B}} \right) \quad (4)$$

The effective widths of the filters are calculated as the integral of the transmission of the filter multiplied by the quantum efficiency of the CCD:

$$\Delta_{filter} = \int T_{filter} \times QE \, d\lambda \quad (5)$$

For the broad band filter $\Delta_B = 1665 \text{ \AA}$; for the narrow band filter $\Delta_N = 173 \text{ \AA}$. The conversion flux-magnitude was done using the spectral energy distribution of Vega given by Castelli & Kurucz (1994).

In Fig. 1 we show the plot for the four surveyed fields showing the curve for flux excess 3σ . Several clear objects exhibiting excess emission are shown. The dashed vertical line is the narrow band limiting magnitude, defined as the m_{NB} that makes $-2.5 \log(1 - 3\sigma(m)) \rightarrow \infty$. Under this magnitude no object can be selected. The solid vertical

Table 2. Objects selected in the field ELAIS a3 with measurements

ID (1)	Coordinates (J2000)		Mag		EW (\AA) (6)	σ exc (7)	CLASS_STAR	
	RA (2)	DEC (3)	I (4)	NB (5)			I (8)	NB (9)
551	16:04:41.4	+54:34:25.52	18.7	18.5	40	5.0	0.02	0.03
561	16:04:43.4	+54:34:35.55	21.9	20.2	1300	4.5	0.02	0.01
1245	16:04:52.8	+54:28:08.54	19.8	19.4	100	4.2	0.04	0.03
1305 ^b	16:04:53.9	+54:28:23.40	19.2	18.9	50	4.4	0.98	0.98
1344 ^b	16:04:54.5	+54:28:16.98	20.1	19.6	100	3.4	0.98	0.98
2247	16:05:06.6	+54:37:59.13	20.0	19.5	110	3.9	0.02	0.03
3420 ^b	16:05:17.9	+54:36:10.93	18.0	17.9	20	3.2	0.98	0.98
4084	16:05:23.9	+54:34:45.12	21.2	20.3	300	3.1	0.00	0.01
5901	16:05:35.1	+54:27:04.54	18.8	18.5	50	7.2	0.03	0.03
6224 ^b	16:05:39.8	+54:26:19.25	18.8	18.7	30	3.3	0.98	0.98
7003 ^a	16:05:46.3	+54:37:12.68	>21.6	20.9	>3000	3.3	0.00	0.44
7224	16:05:47.2	+54:25:57.49	20.1	19.6	120	3.8	0.25	0.04
7227 ^b	16:05:46.3	+54:39:11.74	17.5	17.0	110	13.3	0.36	0.93
7605 ^b	16:05:50.0	+54:38:48.02	18.4	18.2	20	3.8	0.97	0.98
7836	16:05:51.4	+54:32:07.63	18.7	18.5	50	6.4	0.03	0.03
7930	16:05:52.4	+54:33:23.82	20.1	19.6	120	3.7	0.00	0.02
8412	16:05:54.5	+54:38:37.76	18.0	17.9	20	3.1	0.03	0.03
8661	16:06:07.9	+54:35:42.45	19.3	18.9	70	5.6	0.02	0.03
8971	16:06:03.2	+54:30:27.56	20.2	19.8	110	3.0	0.04	0.10
9064 ^a	16:06:03.3	+54:28:11.14	>21.6	20.8	>4000	3.2	0.12	0.02
9668 ^b	16:06:20.8	+54:31:50.12	18.6	18.4	20	3.8	0.19	0.77
9856	16:06:20.3	+54:31:49.59	22.3	20.7	1100	3.1	0.14	0.01
9996 ^b	16:06:12.6	+54:29:42.39	18.2	18.1	30	4.7	0.48	0.92
10108 ^b	16:06:00.5	+54:26:52.75	18.0	17.8	50	7.0	0.97	0.97
10141	16:06:18.1	+54:30:59.20	20.3	19.2	370	9.1	0.18	0.03

^a selected under the broad limit magnitude.

^b catalogued as star.

line is the brighter of the detection-limiting magnitudes on the four fields. Only objects brighter than this limit will be used to obtain the luminosity function.

Table 2 lists the candidates detected in the fields at $\geq 3\sigma$. The first column (1) is the identification number in the catalogue produced by **SExtractor**; (2) and (3) are the coordinates of the object, with an accuracy better than $1''$; (4) and (5) are the magnitudes of the objects inside the apertures, with typical accuracies better than 0.1 magnitudes for both bands; (6) is the the equivalent width measured using eq. 4. The uncertainty is better than 30% for low EWs ($< 400 \text{ \AA}$). (7) is the σ excess of the detection; and (8), (9) are the **CLASS_STAR** parameter produced by **SExtractor** in the *I* and narrow band images.

A total of 52 line-emission candidates were selected in the frames, with an additional 16 objects detected only in the narrow band image. The density of objects selected in both bands is 279 objects per square degree (365 objects per square degree when counting also the objects only detected in the narrow-band image). The objects cover an *I* magnitude range from 17 to 22. In Table 3 the range of variation of several quantities of the objects detected in each field is listed. In Fig. 2 several examples of the detected objects are shown.

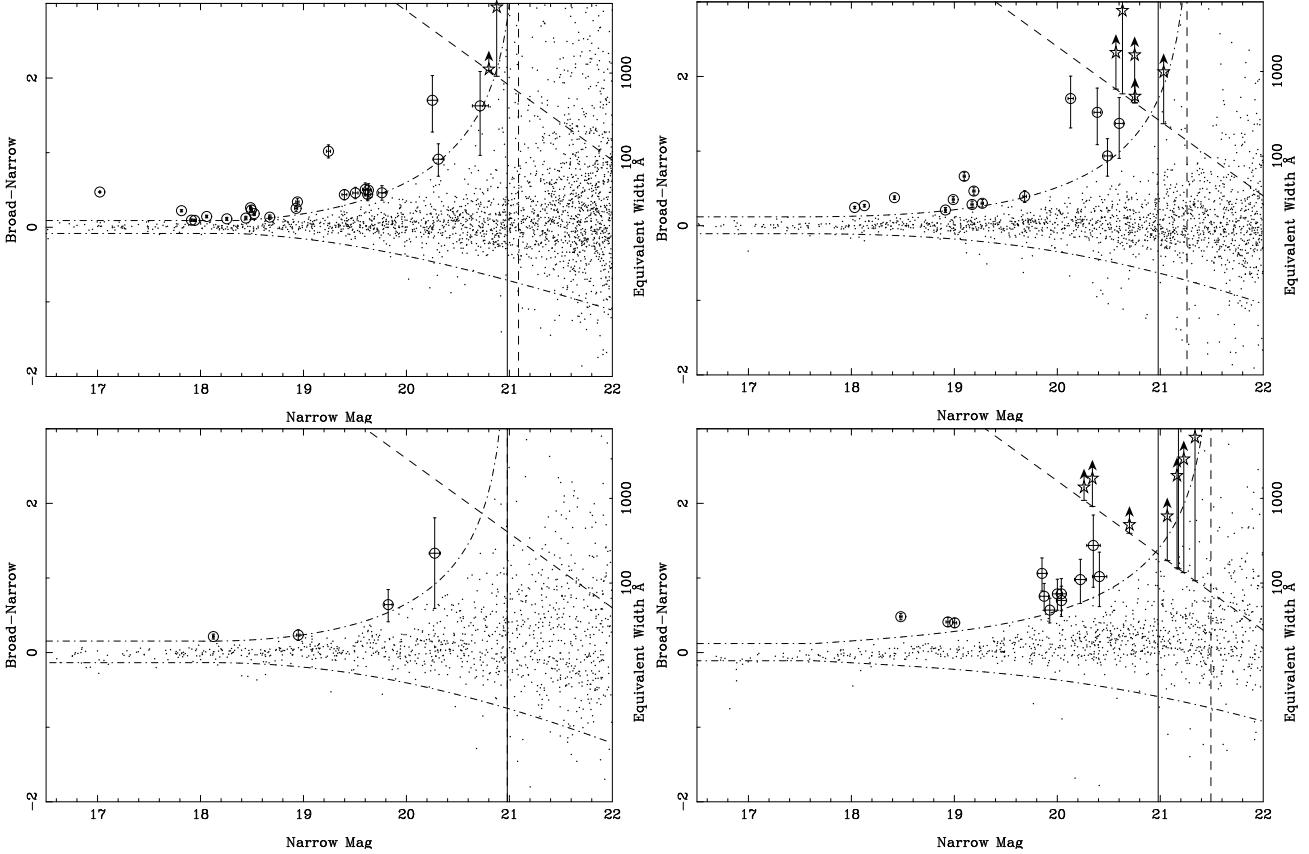


Fig. 1. m_{NB} vs $I - m_{NB}$ for the fields a3, a4, b3 and b4 (from top to bottom and left to right). The dashed curve represents the 3σ detection limit, the diagonal dashed line is the limiting broad magnitude, the dashed vertical line is the limiting narrow magnitude for object selection, and the solid vertical line is the limiting magnitude used in the analysis (i.e., the limiting magnitude for the shallowest field). The star-shaped points with up-pointing arrows are objects selected below the limiting broad band magnitude, i.e., detected in the narrow-band image but only marginally detected in the broad-band image.

3.2. Galaxy – star segregation

The sample can be contaminated by stellar objects (either stars or AGN). To minimise their effect, we have used the parameter `CLASS_STAR` provided by `SExtractor`. We can see in Fig. 3 how this parameter is distributed. Only the candidates selected over the limiting magnitudes are plotted, as `SExtractor` tends to mis-classify dim objects. Our assumption is that all the objects over `CLASS_STAR`=0.5 in at least one of the images are stars (15 objects in the sample). The objects with a large variation of the `CLASS_STAR` parameter from the narrow to the broad-band image were visually inspected, and classified according to their light profiles. Objects classified as stars were excluded from our analysis.

3.3. Contamination from other lines

A narrow band survey of emission line galaxies can potentially detect galaxies with different emission lines at different redshifts. If the source redshift and the rest frame wavelength of the line act to place it inside the narrow band filter, the line will be detected if it is sufficiently strong. The fixed flux detection limit translates to different luminosities for each line given the different redshift

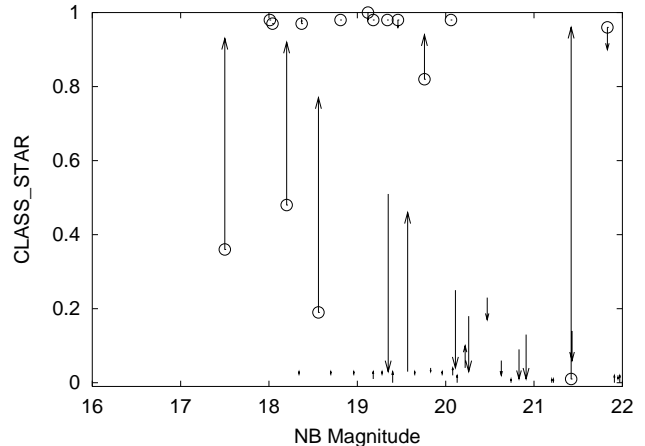


Fig. 3. `CLASS_STAR` versus aperture magnitude in the narrow band. The tail of the arrow is `CLASS_STAR` in the broad band image and the head is `CLASS_STAR` in the narrow band image. The arrows with a circle in the tail are objects selected as stars. There is a clear segregation between low `CLASS_STAR` (non-stellar-like profiles) and high `CLASS_STAR` (stellar-like profiles)

of the galaxies. Furthermore, a different volume is covered for each line for the same reason. The emission lines we

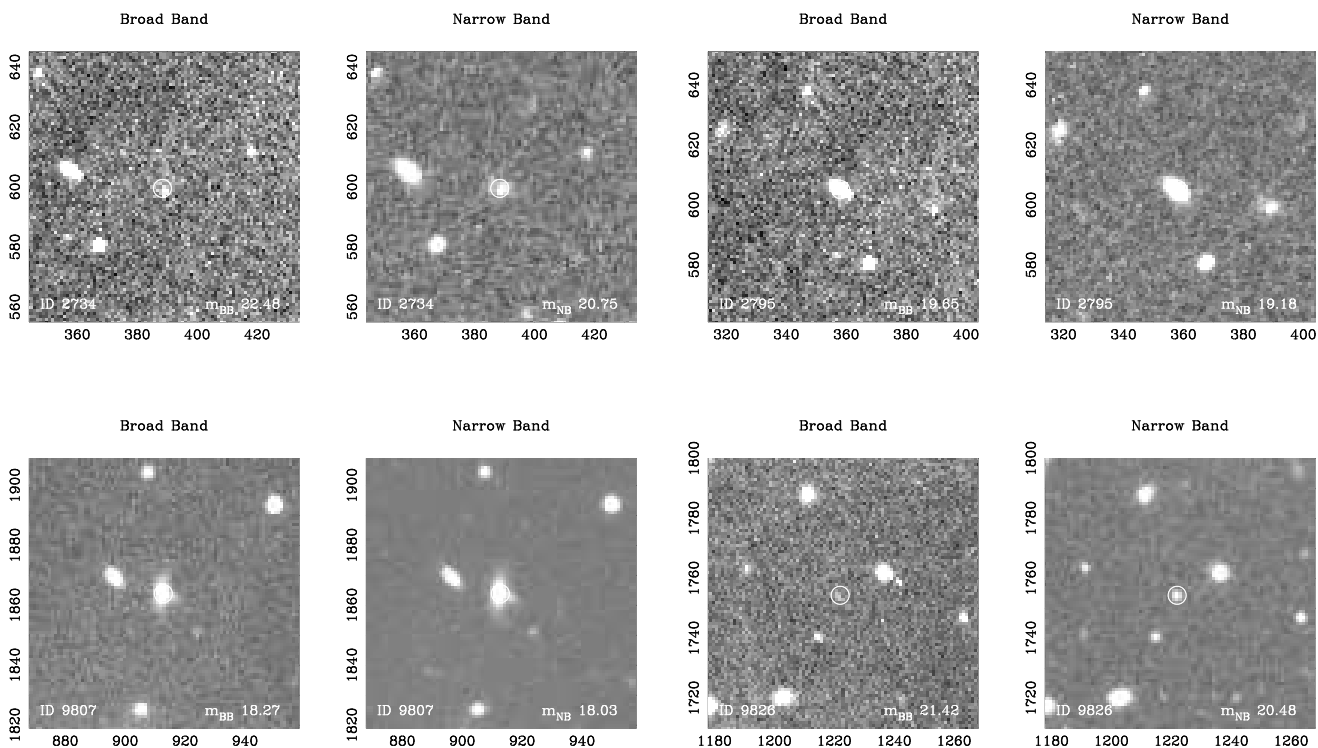


Fig. 2. Sample of selected objects on the field ELAIS-a4. The size of the boxes is 25'', north is on the right, east is upwards. Each figure shows the identification number in the catalogue produced by **SExtractor** (ID) and the apparent magnitude in the band

would expect to detect are H α , H β , [O III] $\lambda\lambda$ 4959, 5007 and [O II] λ 3727 (Tresse et al. 1999; Kennicutt 1992b) as the narrow band filter pass band is too wide to separate [N II] $\lambda\lambda$ 6548, 6584 from H α . In Table 4 we show the different redshift coverage for each line.

Since we do not have spectroscopic redshifts for the candidate, it is necessary to estimate the number of background emission line galaxies likely to appear in the survey. We made estimates of the number of galaxies expected from each of the lines relative to H α (Jones & Bland-Hawthorn 2001). For this purpose we need to know the luminosity function in each line and its evolution with redshift. For H α , this function has been determined at a wide range of redshifts (Gallego et al. 1995; Tresse & Maddox 1998; Yan et al. 1999). We also assume an evolution of the parameters ϕ^* , L^* and α of the form:

$$\phi^*(z) = \phi_0^*(1+z)^{\gamma_\phi} \quad (6)$$

$$L^*(z) = L_0^*(1+z)^{\gamma_L} \quad (7)$$

$$\alpha(z) = \alpha_0 + \gamma_\alpha z \quad (8)$$

using the functional forms adopted by Heyl et al. (1997). The free parameters were constrained using the luminosity function of Gallego et al. (1995) at $z=0$ and Tresse & Maddox (1998) at $z=0.2$. The parameters of the H α

luminosity function are then:

$$\begin{aligned} \phi^*(z) &= 10^{-3.2}(1+z)^{4.68} \text{ Mpc}^{-3} \\ L^*(z) &= 10^{42.15}(1+z)^{-0.25} \text{ erg s}^{-1} \\ \alpha(z) &= -1.3 - 0.25z \end{aligned} \quad (9)$$

As the luminosity functions for the other emission lines have not been determined, our approach was to scale the L^* parameter of the H α luminosity function using mean flux ratios from Kennicutt (1992a), weighted with the relative occurrence of each galaxy type (Jones & Bland-Hawthorn 2001). The values of $\log L^*$ in erg s^{-1} are: $\log L_{[\text{O III}]}^* = 41.97$, $\log L_{\text{H}\beta}^* = 41.69$, $\log L_{[\text{O II}]}^* = 42.63$.

The rest of the parameters of the luminosity function are assumed to be equal to the values of the local H α luminosity function. We have assumed the line ratio $\text{H}\alpha/[\text{N II}]\lambda\lambda$ 6548, 6584=2.3 (obtained by Kennicutt 1992a; Gallego et al. 1997; used by Tresse & Maddox 1998; Yan et al. 1999; Iwamuro et al. 2000).

The mean internal extinction is assumed to be 1 magnitude in H α following Kennicutt (1983), who finds this value for nearby spirals. Also the star-forming galaxies sample from Gallego et al. (1995) has a mean $E(B-V)=0.6$, which yields a mean H α extinction of 1 magnitude. The extinction in the other lines is scaled using the flux ratios and the extinction law of Mathis (1990). These values

Table 2. (cont.) Objects selected in the field ELAIS a4 with measurements

ID	Coordinates (J2000)		Mag		EW (\AA)	σ exc	CLASS_STAR	
	RA	DEC	I	NB			I	NB
723 ^a	16:03:08.7	+54:32:15.68	>21.2	21.0	>700	3.1	0.10	0.01
1427 ^a	16:03:20.1	+54:29:39.68	>21.2	20.6	>2000	4.6	0.99	0.78
2126 ^b	16:03:28.2	+54:37:53.50	19.1	18.9	40	3.1	1.00	0.98
2158 ^b	16:03:28.5	+54:27:39.67	21.8	20.1	1300	5.7	0.96	0.90
2606 ^b	16:03:32.5	+54:27:02.20	19.3	19.0	80	4.7	0.98	0.98
2734 ^a	16:03:33.6	+54:27:13.30	>21.2	20.8	>1000	3.6	0.00	0.00
2795	16:03:34.0	+54:26:57.43	19.6	19.2	110	5.1	0.02	0.03
8242 ^b	16:04:14.6	+54:25:56.00	19.8	19.1	180	7.2	0.82	0.94
8655 ^a	16:04:19.4	+54:27:09.68	>21.2	20.8	>1000	3.9	0.00	0.04
8934	16:04:22.3	+54:27:12.42	21.9	20.4	900	4.5	0.00	0.02
8942	16:04:22.2	+54:27:18.81	22.0	20.6	700	3.6	0.00	0.02
9041 ^a	16:04:23.6	+54:27:07.30	>21.2	20.6	>2000	4.5	0.02	0.04
9381 ^b	16:04:24.7	+54:27:03.65	19.5	19.2	60	3.4	0.98	0.96
9807	16:04:49.8	+54:31:51.03	18.3	18.0	50	5.4	0.03	0.03
9826 ^b	16:04:43.3	+54:34:33.76	21.4	20.5	300	3.2	0.01	0.96
9989	16:04:37.9	+54:34:46.66	18.4	18.1	60	5.8	0.03	0.03
10732	16:04:41.3	+54:34:23.93	18.8	18.4	80	6.9	0.03	0.03
11185	16:04:36.6	+54:36:50.56	20.1	19.7	90	3.1	0.02	0.04
11748	16:04:32.5	+54:30:35.14	19.6	19.3	60	3.4	0.03	0.46

^a selected under the broad limit magnitude.

^b catalogued as star.

Note: a3_551 and a4_10732 are the same object

are 1.78 magnitudes for [O III] $\lambda\lambda$ 4959, 5007, 1.88 for H β and 2.72 for [O II] λ 3727.

Figure 4 shows the predicted cumulative number counts for the H α , H β , [O II] λ 3727 and [O III] $\lambda\lambda$ 4959, 5007 as a function of line flux. The population of H α emitting galaxies clearly dominates at brighter fluxes as a galaxy emitting in other line would be more distant, and hence more luminous and rarer. The flux line where H α emitters are more than 90% of the total number of galaxies is $1.68 \cdot 10^{-16}$ erg s $^{-1}$ cm $^{-2}$. As the minimum line flux of the objects in the sample is $7.22 \cdot 10^{-16}$ erg s $^{-1}$ (corrected from extinction, and the effect of the [N II] $\lambda\lambda$ 6548, 6584 lines), we can be confident that the contamination from other emission lines is negligible.

3.4. Luminosity of the objects

At this stage we assume that we have a sample of H α emitting galaxies. The distribution of equivalent widths and magnitudes of these objects is shown in Fig. 5.

The luminosity of the objects is calculated from their line flux. We correct for the presence of the [N II] $\lambda\lambda$ 6548, 6584 lines, as the narrow filter is unable to separate the contribution of these lines. We also apply a mean internal extinction correction to the objects. For the first two corrections we have assumed the same values used in Sect. 3.3, i.e., H α /[N II] $\lambda\lambda$ 6548, 6584=2.33 and $A_{H\alpha}$ =1. (Note that a wide range of H α /[N II] $\lambda\lambda$ 6548, 6584 ratios is present in star-forming galaxies. In the extreme case of BCD galaxies, H α /[N II] $\lambda\lambda$ 6548, 6584 \sim 20. If the

Table 2. (cont.) Objects selected in the fields ELAIS b3 and b4 with measurements

ID	Coordinates (J2000)		Mag		EW (\AA)	σ exc	CLASS_STAR	
	RA	DEC	I	NB			I	NB
13504	16:05:59.0	+54:13:40.60	20.5	19.8	170	3.4	0.23	0.17
14173 ^a	16:06:10.2	+54:23:42.57	>21.3	19.5	>4000	9.5	0.00	0.96
14456	16:06:13.7	+54:21:48.86	19.2	18.9	50	3.1	0.01	0.03
14658	16:06:18.6	+54:17:10.07	21.6	20.3	600	3.7	0.00	0.00
14820	16:06:20.9	+54:25:30.20	18.3	18.1	40	4.1	0.02	0.03

ID	Coordinates (J2000)		Mag		EW (\AA)	σ exc	CLASS_STAR	
	RA	DEC	I	NB			I	NB
5083	16:03:55.0	+54:20:32.47	20.9	19.9	400	5.1	0.13	0.01
5353	16:03:56.0	+54:19:54.77	20.8	20.0	230	3.8	0.01	0.01
5420	16:03:56.6	+54:19:56.00	20.8	20.0	230	3.8	0.09	0.01
5465 ^a	16:03:57.2	+54:20:53.35	>22.3	20.3	>3000	5.6	0.38	0.01
5526 ^a	16:03:57.8	+54:18:15.48	>22.3	21.2	>400	3.7	0.00	0.00
6574 ^a	16:04:01.8	+54:22:32.49	>22.3	20.3	>2000	5.4	0.03	0.01
6643	16:04:01.2	+54:22:31.65	19.4	18.9	90	4.2	0.51	0.03
6733	16:04:02.6	+54:21:20.63	20.6	19.9	220	4.0	0.06	0.02
7302 ^a	16:04:07.6	+54:17:37.15	>22.3	21.2	>400	3.2	0.00	0.00
7323	16:04:06.5	+54:23:58.02	21.8	20.4	800	4.5	0.00	0.00
8696 ^a	16:04:20.7	+54:16:08.42	>22.3	21.2	>500	3.3	0.11	0.06
9146 ^a	16:04:28.1	+54:13:40.33	>22.3	21.1	>500	3.2	0.00	0.00
9528	16:04:32.2	+54:22:09.57	19.4	19.0	90	4.0	0.00	0.03
11002	16:04:51.5	+54:14:36.91	20.5	19.9	140	3.2	0.00	0.00
11594	16:04:59.0	+54:26:33.56	20.7	20.0	190	3.5	0.00	0.01
11643	16:04:58.8	+54:17:00.85	19.0	18.5	120	6.2	0.02	0.03
11683	16:05:00.5	+54:17:00.68	21.2	20.2	300	3.9	0.00	0.01
12527	16:05:13.1	+54:15:39.45	21.4	20.4	400	3.6	0.14	0.06
12850 ^a	16:05:16.6	+54:25:15.15	>22.3	20.7	>1000	3.9	0.03	0.01
13336 ^a	16:05:20.5	+54:16:18.10	>22.3	21.3	>300	3.1	0.01	0.00

^a selected under the broad limit magnitude.

^b catalogued as star.

Table 3. Number of objects detected in each field

Field ELAIS	#	I mag		m _{NB}		EW		Limit Mag	
		range	range	range	range (\AA)	I	m _{NB}		
a3	23	17.5–22.3	17.0–20.7	20	1300	22.9	24.2		
a4	14	17.2–20.8	18.0–20.6	40	1300	22.5	24.8		
b3	4	18.3–21.6	18.1–20.3	40	600	22.6	24.3		
b4	12	19.0–21.8	18.5–20.4	90	800	22.5	24.0		

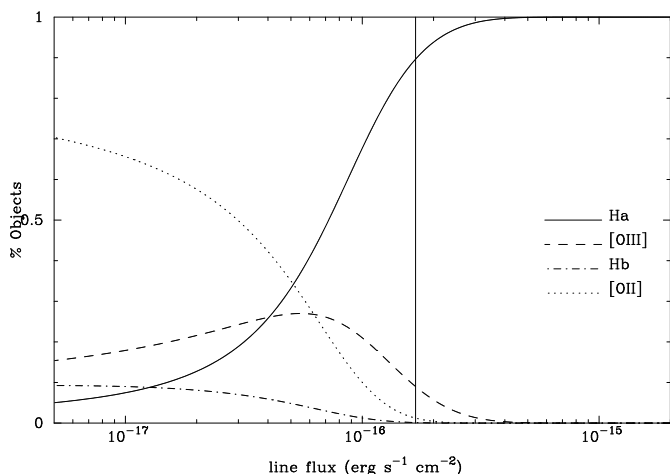
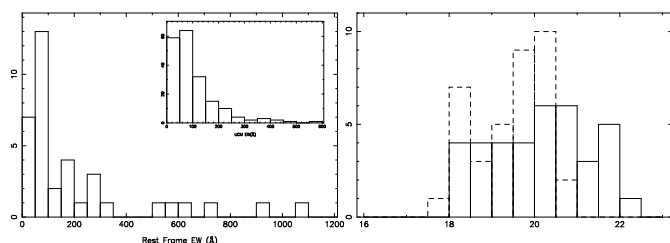
Note: Only objects detected in both bands included in the ranges.

entire sample of detected objects were BCD galaxies, a overall increase of the luminosity density of a factor ~ 1.4 would occur). We also apply a small statistical correction (8%) to the measured flux due to the fact that the filter is not square in shape. Due the small apparent size of the objects, it is not necessary to make an aperture correction. The corrected H α flux is given by:

$$f_0(\text{H}\alpha) = f(\text{H}\alpha) \frac{\text{H}\alpha}{\text{H}\alpha + [\text{N II}]\lambda\lambda 6548, 6584} 10^{0.4A_{\text{H}\alpha}} \times 1.08 (10)$$

Table 4. Emission lines potentially detected inside the narrow band

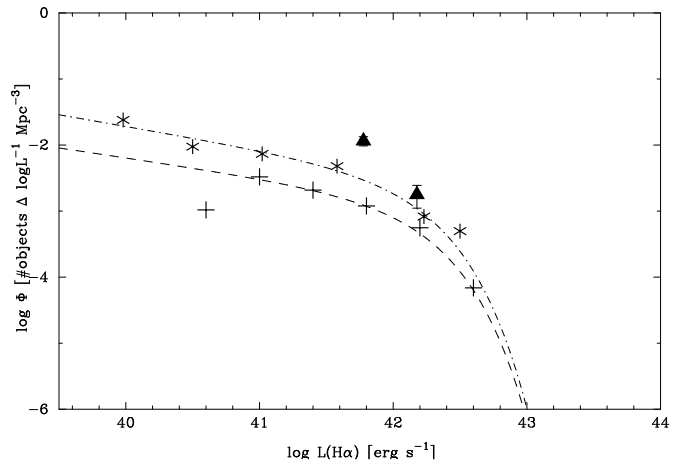
Line	Redshift range		\bar{z}	d_c^a (Mpc)	$V \times 10^4^b$ (Mpc 3)
	$z_1 \leq z \leq z_2$				
H α	0.228	0.256	0.242	1230	0.98
[O III] $\lambda\lambda$ 4959, 5007	0.610	0.645	0.628	2590	3.81
H β	0.659	0.694	0.676	2730	4.17
[O II] λ 3727	1.16	1.20	1.18	3870	7.34

^a Comoving distance^b Comoving volume**Fig. 4.** Cumulative number counts for H α , H β , [O II] λ 3727 and [O III] $\lambda\lambda$ 4959, 5007 emitting galaxies expected in our sample (see text for details). The vertical line shows the line flux in which H α galaxies represent more than 90% of the total ($1.68 \cdot 10^{-16} \text{ erg s}^{-1}$)**Fig. 5.** **a)** (left panel) Histogram of the rest frame EWs of our objects. The histogram of the EWs for UCM survey galaxies is shown in the inset. **b)** (right panel) Histogram of the broad band and narrow band magnitudes of the objects selected in both bands. The I magnitudes are represented by solid lines, m_{NB} by dashed lines

Finally the H α luminosity is given by:

$$L(\text{H}\alpha) = 4\pi d_l^2(z) f_0(\text{H}\alpha) \quad (11)$$

using the redshift of the line at the centre of the filter $z=0.242$ and d_l the luminosity distance, defined from the comoving distance as $d_l = (1+z)d_c$.

**Fig. 6.** Luminosity function of the selected objects (filled triangles), compared with the luminosity functions and Schechter best fit of Gallego et al. (1995) (LF crosses, Schechter fit dashed line) and Tresse & Maddox (1998) (LF asterisks, Schechter fit dot-dashed line). Error bars indicate Poisson uncertainties only

4. Luminosity function and star formation rates

4.1. Galaxy luminosity function

Direct information of the amount and distribution of the SFR can be obtained by constructing the luminosity function for galaxies with star formation activity. With all the objects in a small range of redshifts (Table 4), the luminosity function will be given by:

$$\Phi(\log L_i) = \frac{1}{\Delta \log L} \sum_j \frac{1}{V(z)_j} \quad (12)$$

with $|\log L_j - \log L_i| < \Delta \log L$

where $V(z)_j$ is the volume of the narrow slice in redshift covered by the filter. We have taken into account the filter shape in the computation of the volume. The correction can be as large as 25% for the faintest galaxies (as compared to a square filter).

The summation is over all the galaxies in the H α luminosity range $\log L(\text{H}\alpha) \pm \Delta \log L(\text{H}\alpha)$. We have used $\Delta \log L(\text{H}\alpha) = 0.4$ (i.e., one magnitude). Figure 6 shows the luminosity function, compared with the luminosity functions of Gallego et al. (1995) and Tresse & Maddox (1998).

4.2. Luminosity density and star formation rate density

The H α luminosity density can be obtained integrating the luminosity function:

$$\mathcal{L} = \int_0^\infty \phi^* L \left(\frac{L}{L^*} \right)^\alpha \exp \left(-\frac{L}{L^*} \right) d \left(\frac{L}{L^*} \right) \quad (13)$$

Given the small luminosity range covered by our objects, we can not fit a Schechter function. We assume a shape (α and L^*) for the luminosity function, and obtain the total luminosity density from the summed luminosity density of the objects in the sample, extrapolating using the assumed LF outside the observed range. We use the

H α luminosity function at $z=0$ obtained by Gallego et al. (1995) in this exercise. The line flux of the faintest object ($7.22 \cdot 10^{-16}$ erg s $^{-1}$ cm $^{-2}$) translates into a H α luminosity of $3.78 \cdot 10^{41}$ erg s $^{-1}$. The surveyed volume is $9.8 \cdot 10^3$ Mpc 3 . The summed luminosity density (\mathcal{L}_{sum}) in our sample is $(3.3 \pm 0.7) \cdot 10^{39}$ erg s $^{-1}$ Mpc $^{-3}$. Thus, the total luminosity density can be written as:

$$\mathcal{L} = \mathcal{L}_{sum} \frac{\int_0^\infty L \left(\frac{L}{L^*}\right)^\alpha \exp\left(-\frac{L}{L^*}\right) d\left(\frac{L}{L^*}\right)}{\int_{L_{lim}}^\infty L \left(\frac{L}{L^*}\right)^\alpha \exp\left(-\frac{L}{L^*}\right) d\left(\frac{L}{L^*}\right)} \quad (14)$$

Using the incomplete gamma function³ finally we obtain:

$$\mathcal{L} = \mathcal{L}_{sum} \frac{1}{1 - \gamma(x, 2 + \alpha)} \quad \text{with } x = \frac{L_{lim}}{L^*} = 0.27 \quad (15)$$

The total luminosity density is then $(5.4 \pm 1.1) \cdot 10^{39}$ erg s $^{-1}$ Mpc $^{-3}$. Note that using the luminosity function of Tresse & Maddox (1998) produces a luminosity density of $(5.9 \pm 1.2) \cdot 10^{39}$ erg s $^{-1}$ Mpc $^{-3}$. The difference is small ($\sim 10\%$) and inside the error bars. In principle, not all the H α luminosity is produced by star formation. The Active Galactic Nuclei can also contribute to the luminosity. The amount of this contribution is 8% of the number of galaxies and 15% of the luminosity density for the UCM sample of H α emitting galaxies. Assuming no evolution in the contribution to H α from AGN, the luminosity density corrected from the AGN contribution is $(4.7 \pm 0.9) \cdot 10^{39}$ erg s $^{-1}$ Mpc $^{-3}$.

The star formation rate can be estimated from the H α luminosity using (Kennicutt 1998):

$$SFR_{H\alpha}(M_\odot \text{yr}^{-1}) = 7.9 \cdot 10^{-42} L(\text{H}\alpha) (\text{erg s}^{-1}) \quad (16)$$

Thus, the H α luminosity density translates into a SFR density of $(0.043 \pm 0.009) M_\odot \text{yr}^{-1} \text{Mpc}^{-3}$ (with AGN correction $(0.037 \pm 0.009) M_\odot \text{yr}^{-1} \text{Mpc}^{-3}$). Figure 7 shows the evolution of the SFR density of the Universe from $z=0$ to $z=2.2$ measured using Balmer lines. The right axis shows the luminosity density and the left axis the SFR. All the points have been computed using the same SFR-luminosity conversion factor and the point from Gallego et al. (1995) was computed *with* the AGN contribution.

The H α luminosity is sensitive only to star formation in stars over $10M_\odot$, which are the main contributors to the ionising flux. The SFR density given here is thus an extrapolation assuming a given IMF. The conversion factor between H α luminosity density and SFR density is thus very sensitive to the IMF, metallicity and details of the population synthesis models used (Glazebrook et al. 1999). It is thus very important to be consistent when comparing different SFR density estimates from the literature. In Fig. 7 we have taken the measured H α luminosity densities and transformed them into SFR densities using the same transformation given above.

The SFR density measured here is lower than that of Jones & Bland-Hawthorn (2001). At their lower flux cut-off at $z \sim 0.2$ ($0.5 \cdot 10^{-16}$ erg s $^{-1}$ Mpc $^{-3}$) there is a noticeable contamination from [O III] $\lambda\lambda 4959, 5007$ and H β (see

³ defined as $\gamma(x, \alpha) = \frac{1}{\Gamma(\alpha)} \int_0^x u^{\alpha-1} e^{-u} du$

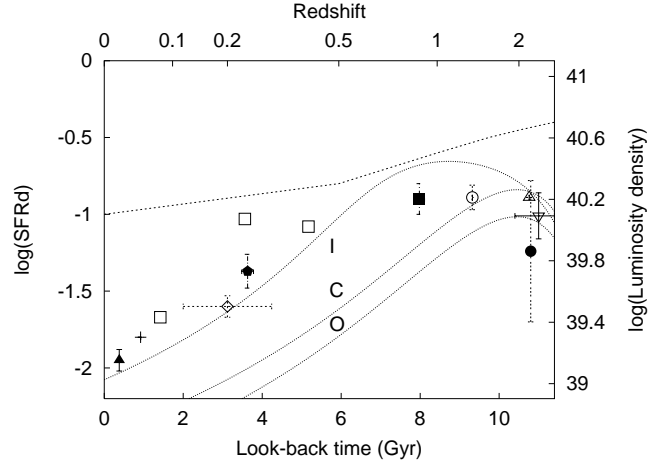


Fig. 7. Evolution of the SFR density measured with Balmer recombination lines. H α points are from Gallego et al. (1995) (filled triangle), Gronwall (1999) (cross), Tresse & Maddox (1998) (diamond), this work (filled pentagon), Jones & Bland-Hawthorn (2001) (open squares), Glazebrook et al. (1999) (filled square), Yan et al. (1999) (open circle), Iwamuro et al. (2000) (open triangle), Moorwood et al. (2000) (filled circle); H β point is Pettini et al. (1998) (inverted triangle). The top dotted line corresponds to the model of Somerville & Primack (1998); the rest of the dotted lines are the inflow (I), closed-box (C) and outflow (O) models from Pei & Fall (1995)

Fig 4). The technique used (tunable filters) implies a very low minimum detected EW ($\sim 5\text{\AA}$). Consequently, more objects are detected (either low EW H α , not detected in our survey or [O III] $\lambda\lambda 4959, 5007$ and H β emitting galaxies classified as H α). This could explain the very high SFR found by Jones & Bland-Hawthorn (2001) compared to our result. Another important result at $z \sim 0.2$ is that given by Tresse & Maddox (1998). They measured spectroscopic H α + [N II] $\lambda\lambda 6548, 6584$ fluxes of the *I*-selected CFRS galaxies lying at redshift below 0.3. Because of the *I* selection, these galaxies have been selected by light from the old stellar population, rather than from their young stars. This sample is less sensitive to galaxies undergoing recent star formation than are H α (or *B*) selected surveys. Also, the width of the *I* filter does not favor the detection of galaxies with strong H α emission. Despite these differences, our results are consistent with the strong increase in the SFR density from $z = 0$ to $z = 1$.

Several theoretical models are also plotted in Fig 7. Semianalytic models of galaxy formation and evolution (Somerville & Primack 1998) have difficulties in predicting such steep evolution, while other approaches like that of Pei & Fall (1995) have more success. It is beyond the scope of this paper to discuss these theoretical models in any detail since our main concern is to present the observational results.

5. Summary and conclusions

We have carried out a survey searching for H α emitting galaxies at $z \simeq 0.24$ using a narrow band filter tuned with

the redshifted line. The total sky area covered was 0.19 square degrees within the redshift range 0.228 to 0.255, corresponding to a volume of $9.8 \cdot 10^3 \text{ Mpc}^3$ and a look-back time of 3.6 Gyr ($H_0 = 50 \text{ km s}^{-1} \text{ Mpc}^{-1}$ and $q_0 = 0.5$).

A total of 52 objects were selected as candidates for a broad-band limiting magnitude of $I \sim 22.9$, plus 16 objects detected only in the narrow-band image for a narrow band limiting magnitude for object detection of 21.0. The threshold detection corresponds to about 20Å equivalent width with an uncertainty of $\sim \pm 10\text{Å}$. After excluding point-like objects from our analysis, a sample of 47 emission line galaxies was produced, 37 of which were detected in both the narrow-band and broad-band filters. The minimum line flux in the sample is $7.22 \cdot 10^{-16} \text{ erg s}^{-1} \text{ cm}^{-2}$, corresponding to a minimum H α luminosity of $3.8 \cdot 10^{41} \text{ erg s}^{-1}$.

In the absence of spectroscopic confirmation, we have estimated the likely contamination from other emission lines such as [O II] $\lambda 3727$, H β and [O III] $\lambda\lambda 4959, 5007$ at redshifts 1.2, 0.66 and 0.61 respectively, and found it to be negligible at the relatively high flux limits of our sample.

We find an extinction-corrected H α luminosity density of $(5.4 \pm 1.1) \cdot 10^{39} \text{ erg s}^{-1} \text{ Mpc}^{-3}$. This uncertainty takes into account the photometric and Poissonian errors only. Assuming a constant relation between the H α luminosity and star formation rate, the SFR density in the covered volume is $(0.043 \pm 0.009) \text{ M}_\odot \text{ yr}^{-1} \text{ Mpc}^{-3}$. This translates to $(0.037 \pm 0.009) \text{ M}_\odot \text{ yr}^{-1} \text{ Mpc}^{-3}$ when the total density is corrected for the AGN contribution as estimated in the local Universe. This value is a factor ~ 4 higher than the local SFR density, and consistent with the strong increase in the SFR density from $z = 0$ to $z = 1$ previously reported, although our results will have to be confirmed by future spectroscopic follow-up observations.

Acknowledgements. This paper is based on observations obtained at the German-Spanish Astronomical Centre, Calar Alto, Spain, operated by the Max-Planck Institute für Astronomie (MPIE), Heidelberg, jointly with the Spanish Commission for Astronomy. This research was supported by the Spanish *Programa Nacional de Astronomía y Astrofísica* under grant AYA2000-1790. S. Pascual acknowledges the receipt of a *Formación de Profesorado Universitario* fellowship from the Universidad Complutense de Madrid. A. Aragón-Salamanca acknowledges generous financial support from the Royal Society. This work has benefitted from fruitful discussions with C. E. García-Dabó and P. G. Pérez-González.

References

- Baugh, C. M., Cole, S., Frenk, C. S., & Lacey, C. G. 1998, ApJ, 498, 504+
- Bertin, E. & Arnouts, S. 1996, A&AS, 117, 393
- Castelli, F. & Kurucz, R. L. 1994, AAP, 281, 817
- Charlot, S. 1998, in *The Next Generation Space Telescope: Science Drivers and Technological Challenges*, 135+
- Cole, S., Aragon-Salamanca, A., Frenk, C. S., Navarro, J. F., & Zepf, S. E. 1994, MNRAS, 271, 781+
- Ellis, R. S., Colless, M., Broadhurst, T., Heyl, J., & Glazebrook, K. 1996, MNRAS, 280, 235
- Gallagher, J. S., Hunter, D. A., & Bushouse, H. 1989, AJ, 97, 700
- Gallego, J., Zamorano, J., Aragon-Salamanca, A., & Rego, M. 1995, ApJL, 455, L1
- Gallego, J., Zamorano, J., Rego, M., & Vitores, A. G. 1997, ApJ, 475, 502+
- Glazebrook, K., Blake, C., Economou, F., Lilly, S., & Colless, M. 1999, MNRAS, 306, 843
- Gronwall, C. 1999, in *After the Dark Ages: When Galaxies were Young (the Universe at $2 < z < 5$)*. 9th Annual October Astrophysics Conference in Maryland held 12-14 October, 1998. College Park, Maryland. Edited by S. Holt and E. Smith. American Institute of Physics Press, 1999, p. 335, 335+
- Hammer, F., Flores, H., Lilly, S. J., Crampton, D., Le Fevre, O., Rola, C., Mollen-Ornelas, G., Schade, D., & Tresse, L. 1997, ApJ, 481, 49+
- Heyl, J., Colless, M., Ellis, R. S., & Broadhurst, T. 1997, MNRAS, 285, 613
- Hogg, D. W., Cohen, J. G., Blandford, R., & Pahre, M. A. 1998, ApJ, 504, 622+
- Iwamuro, F., Motohara, K., Maihara, T., Iwai, J., Tanabe, H., Taguchi, T., Hata, R., Terada, H., Oya, M. G. S., Iye, M., Yoshida, M., Karoji, H., Ogasawara, R., & Sekiguchi, K. 2000, PASJ, 52, 73+
- Jones, D. H. & Bland-Hawthorn, J. 2001, ApJ, 550, 593
- Kauffmann, G., Colberg, J. M., Diaferio, A., & White, S. D. M. 1999, MNRAS, 303, 188
- Kauffmann, G., Guiderdoni, B., & White, S. D. M. 1994, MNRAS, 267, 981+
- Kauffmann, G., White, S. D. M., & Guiderdoni, B. 1993, MNRAS, 264, 201+
- Kennicutt, R. C. 1983, ApJ, 272, 54
- . 1992a, ApJ, 388, 310
- . 1992b, ApJS, 79, 255
- . 1998, ARAA, 36, 189
- Lacey, C. & Silk, J. 1991, ApJ, 381, 14
- Lilly, S. J., Le Fevre, O., Hammer, F., & Crampton, D. 1996, ApJL, 460, L1
- Madau, P., Ferguson, H. C., Dickinson, M. E., Giavalisco, M., Steidel, C. C., & Fruchter, A. 1996, MNRAS, 283, 1388
- Mathis, J. S. 1990, ARAA, 28, 37
- Monet, D., Bird, A., Canzian, B., Harris, H., Reid, N., Rhodes, A., Sell, S., Ables, H., Dahn, C., Guetter, H., Henden, A., Leggett, S., Levison, H., Luginbuhl, C., Martini, J., Monet, A., Pier, J., Riepe, B., Stone, R., Vrba, F., & Walker, R. 1996, USNO-A2.01 (U.S. Naval Observatory, Washington DC)
- Moorwood, A. F. M., van der Werf, P. P., Cuby, J. G., & Oliva, E. 2000, AAP, 362, 9
- Oliver, S., Rowan-Robinson, M., Alexander, D. M., Almaini, O., Balcells, M., Baker, A. C., Barcons, X., Barden, M., Bellas-Velidis, I., Cabrera-Guerra, F., Carballo, R., Cesarsky, C. J., Ciliegi, P., Clements, D. L., Crockett, H., Danese, L., Dapergolas, A., Drolia,

- B., Eaton, N., Efstathiou, A., Egami, E., Elbaz, D., Fadda, D., Fox, M., Franceschini, A., Genzel, R., Goldschmidt, P., Graham, M., Gonzalez-Serrano, J. I., Gonzalez-Solares, E. A., Granato, G. L., Gruppioni, C., Herbstmeier, U., Héraudeau, P., Joshi, M., Kontizas, E., Kontizas, M., Kotilainen, J. K., Kunze, D., La Franca, F., Lari, C., Lawrence, A., Lemke, D., Linden-Vørnle, M. J. D., Mann, R. G., Márquez, I., Masegosa, J., Mattila, K., McMahon, R. G., Miley, G., Missoulis, V., Mobasher, B., Morel, T., Nørgaard-Nielsen, H., Omont, A., Papadopoulos, P., Perez-Fournon, I., Puget, J. ., Rigopoulou, D., Rocca-Volmerange, B., Serjeant, S., Silva, L., Sumner, T., Surace, C., Vaisanen, P., van der Werf, P. P., Verma, A., Vigroux, L., Villar-Martin, M., & Willott, C. J. 2000, MNRAS, 316, 749
- Pei, Y. C. & Fall, S. M. 1995, ApJ, 454, 69+
- Pettini, M., Kellogg, M., Steidel, C. C., Dickinson, M., Adelberger, K. L., & Giavalisco, M. 1998, ApJ, 508, 539
- Pettini, M., Shapley, A. E., Steidel, C. C., Cuby, J. G., Dickinson, M., Moorwood, A. F. M., Adelberger, K. L., & Giavalisco, M. 2001, ApJ, 554, 2, in press
- Pickles, A. J. 1998, PASP, 110, 863
- Rowan-Robinson, M., Oliver, S., Efstathiou, A., Gruppioni, C., Serjeant, S., Cesarsky, C. J., Danese, L., Franceschini, A., Genzel, R., Lawrence, A., Lemke, D., McMahon, R., Miley, G., Perez-Fournon, I., Puget, J. L., Rocca-Volmerange, B., Ciliegi, P., Héraudeau, P., Surace, C., Lafranca, F., & Elais Consortium. 1999, ESA SP-427: The Universe as Seen by ISO, 427, 1011+
- Somerville, P. R. & Primack, J. R. 1998, in Birth of Galaxies, ed. G. et al., Xth Rencontre de Blois
- Somerville, R. S., Primack, J. R., & Faber, S. M. 2001, MNRAS, 320, 504+
- Songaila, A., Cowie, L. L., Hu, E. M., & Gardner, J. P. 1994, ApJS, 94, 461
- Tresse, L., Maddox, S., Loveday, J., & Singleton, C. 1999, MNRAS, 310, 262
- Tresse, L. & Maddox, S. J. 1998, ApJ, 495, 691+
- van der Werf, P. P., Moorwood, A. F. M., & Bremer, M. N. 2000, AAP, 362, 509
- Yan, L., McCarthy, P. J., Freudling, W., Teplitz, H. I., Malumuth, E. M., Weymann, R. J., & Malkan, M. A. 1999, ApJL, 519, L47